UC Berkeley

UC Berkeley Previously Published Works

Title

Stochastic generation of MAC waves and implications for convection in Earth's core

Permalink

https://escholarship.org/uc/item/6xb9c6n8

Journal

Geophysical Journal International, 212(3)

ISSN

0956-540X

Authors

Buffett, Bruce
Knezek, Nicholas

Publication Date

2018-03-01

DOI

10.1093/gji/ggx492

Peer reviewed

eScholarship.org Powered by the California Digital Library
University of California

Geophysical Journal International

Geophys. J. Int. (2018) **212,** 1523–1535
Advance Access publication 2017 November 14
GJI Geomagnetism, rock magnetism and palaeomagnetism

doi: 10.1093/gji/ggx492

Stochastic generation of MAC waves and implications for convection in Earth's core

Bruce Buffett and Nicholas Knezek

Department of Earth and Planetary Sciences, University of California, Berkeley, CA 94720*, USA. E-mail: bbuffett@berkeley.edu*

Accepted 2017 November 13. Received 2017 November 8; in original form 2017 August 15

SUMMARY

Convection in Earth's core can sustain magnetic-Archemedes-Coriolis (MAC) waves through a variety of mechanisms. Buoyancy and Lorentz forces are viable sources for wave motion, together with the effects of magnetic induction. We develop a quantitative description for zonal MAC waves and assess the source mechanisms using a numerical dynamo model. The largest sources at conditions accessible to the dynamo model are due to buoyancy forces and magnetic induction. However, when these sources are extrapolated to conditions expected in Earth's core, the Lorentz force emerges as the dominant generation mechanism. This source is expected to produce wave velocities of roughly 2 km yr^{-1} when the internal magnetic field is characterized by a dimensionless Elsasser number of roughly $\Lambda \approx 10$ and the root-mean-square convective velocity defines a magnetic Reynolds number of $Rm \approx 10^3$. Our preferred model has a radially varying stratification and a constant (radial) background magnetic field. It predicts a broad power spectrum for the wave velocity with most power distributed across periods from 30 to 100 yr.

Key words: Composition and structure of the core; Geomagnetic induction; Rapid time variations.

1 INTRODUCTION

Detection of low-frequency magnetic-Archemedes-Coriolis (MAC) waves in a stratified layer at the top of Earth's core conveys information about deeper processes inside the core. Convection is likely the main source of wave excitation, either through buoyant parcels rising into the layer or through electromagnetic disturbances associated with the magnetic field in Earth's core. The amplitude of the response for a given source depends on the damping of the waves. Because MAC waves are damped primarily by molecular rather than turbulent processes (Braginsky 1993), a simple relationship can be established between the excitation source and the wave amplitude (Houdek *et al.* 1999). Wave amplitudes of a few km yr^{-1} are inferred from observations at long wavelengths (Buffett 2014), establishing the required level of excitation and providing valuable insights into the nature of convection.

Wave generation by turbulent motion is commonly represented as a stochastic process (Farrell & Ioannou 1993). Realizations of the stochastic process can be used as an explicit forcing in the governing equations (e.g. Gillet *et al.* 2017). Alternatively, the statistical properties of the excitation source can be related directly to the statistical properties of the waves. The latter approach is most tractable in the Fourier transform domain because it is straightforward to accommodate general descriptions of the excitation source (Rice 1954). In this study we use numerical dynamo models to develop a statistical description of the excitation sources associated with convection and magnetic-field generation in the core across the MAC-wave frequencies. We then use the resulting power spectra to assess the expected wave amplitudes.

A question that naturally arises in using numerical dynamo models is whether the numerical models provide an adequate description of processes in Earth's core. It is often assumed that the models capture the relevant dynamics once the fluid motion evolves into a three-way force balance between magnetic, Archimedes (buoyancy) and Coriolis forces (Christensen *et al.* 2010; Yadav *et al.* 2016). However, there is no assurance that the amplitudes of the individual forces achieve Earth-like values. A recent study of Aubert *et al.* (2017) confronts this question by formulating a strategy for extrapolating numerical solutions to Earth-like conditions while maintaining the so-called MAC force balance. A surprising outcome of applying this general approach to the problem of MAC waves is that the dominant source terms from the dynamo model have a greatly reduced role once the results are extrapolated to more realistic conditions for Earth's core. Instead, the weakest source term (due to magnetic stresses) emerges as the primary mechanism for wave generation because it decreases less rapidly than the other sources over the extrapolation. With reasonable estimates for parameters at core conditions, the predicted level of magnetic stress is sufficient to explain the observed amplitude of the waves. Thus the detection of MAC waves offers an independent and unexpected constraint on magnetic-field generation inside the core.

© The Author(s) 2017. Published by Oxford University Press on behalf of The Royal Astronomical Society.

Downloaded from https://academic.oup.com/gji/article-abstract/212/3/1523/4628047
by University of California, Berkeley/LBL user
on 19 January 2018

This paper is organized as follows. We begin in Section 2 with a description of MAC waves generated by a combination of buoyancy and electromagnetic disturbances. In Section 3 we use a numerical dynamo model to construct a simple stochastic description of the source terms. We use this stochastic model in Section 4 to predict the amplitude of MAC waves. In Section 5 these results are extrapolate to Earth-like conditions. Section 6 outlines the main conclusions.

2 GENERATION OF MAC WAVES

MAC waves arise from an interplay between magnetic, buoyancy and Coriolis forces in a region of stable stratification. Convection and magnetic-field generation in the interior of the core is expected to serve as the main source for the waves. These waves can be represented as small perturbations in density, ρ', pressure, p, velocity, $\mathbf{v}$, and magnetic field, $\mathbf{b}$, which are superimposed on background fields, $\bar{\rho}$, $\bar{P}$, $\bar{\mathbf{V}}$, and $\bar{\mathbf{B}}$. The complete fields are defined by $\mathbf{V} = \bar{\mathbf{V}} + \mathbf{v}$, etc. When the region of stable stratification is thin compared with the characteristic length scale of the background fields, we can assume that $\bar{\mathbf{V}} \cdot \nabla \mathbf{v} \gg \mathbf{v} \cdot \nabla \bar{\mathbf{V}}$. Similar approximations are adopted for the other nonlinear terms. With these assumptions the linearized equations for $\mathbf{v}$ and $\mathbf{b}$ become

$$\frac{\bar{D}\mathbf{v}}{Dt} + 2\boldsymbol{\Omega} \times \mathbf{v} = -\frac{1}{\bar{\rho}}\nabla p + \frac{1}{\bar{\rho}\mu}\bar{\mathbf{B}} \cdot \nabla \mathbf{b} + \frac{\rho'}{\bar{\rho}}\mathbf{g}, \tag{1}$$

$$\frac{\bar{D}\mathbf{b}}{Dt} = \bar{\mathbf{B}} \cdot \nabla \mathbf{v} + \eta \nabla^2 \mathbf{b}, \tag{2}$$

$$\nabla \cdot \mathbf{v} = \nabla \cdot \mathbf{b} = 0, \tag{3}$$

where

$$\frac{\bar{D}()}{Dt} = \frac{\partial()}{\partial t} + \bar{\mathbf{V}} \cdot \nabla(), \tag{4}$$

denotes the material derivative associated with the background flow. Here $\boldsymbol{\Omega}$ is the rotation vector, μ is the magnetic permeability, $\mathbf{g} = -g\hat{\mathbf{r}}$ is the acceleration due to gravity, and η is the magnetic diffusivity. Adopting a Boussinesq approximation in the complementary equations for convection (e.g. Jones 2011) means that $\bar{\rho}$ in (1) can be replaced with a constant reference density ρ_0.

Density variations are necessarily retained in the buoyancy force. For the wave problem, the density perturbation in (1) arises solely from motion of fluid parcels through the background density profile. In an incompressible fluid we require

$$\frac{\partial \rho'}{\partial t} + \mathbf{v} \cdot \nabla \bar{\rho} = 0, \tag{5}$$

where the gradient in the background density is primarily in the radial direction (i.e. $\nabla \bar{\rho} \approx \partial_r \bar{\rho}\, \hat{\mathbf{r}}$). Convective fluctuations also contribute to the local density perturbation, but these variations are treated separately as part of the source term for the waves.

A quantitative description of source mechanism depends on the details of the background flow. Lighthill (1952) addressed this question by writing the governing equations for the complete fields in terms of the linear (wave) equations from (1) to (3) for a fluid that is otherwise at rest ($\bar{\mathbf{V}} = 0$) plus a correction term. For example, the momentum equation for $\mathbf{V}$ in the Boussinesq approximation can be written as

$$\frac{\partial \mathbf{V}}{\partial t} + 2\boldsymbol{\Omega} \times \mathbf{V} = -\frac{1}{\rho_0}\nabla P + \frac{1}{\rho_0 \mu}\bar{\mathbf{B}} \cdot \nabla \mathbf{b} + \frac{\rho'}{\rho_0}\mathbf{g} + \Phi, \tag{6}$$

where Φ represents the correction term. Both ρ' and $\mathbf{b}$ should interpreted as terms due solely to wave motion (e.g. ρ' should obey eq. 5).

In order for (6) to accurately describe the momentum equation for $\mathbf{V}$ we require

$$\Phi = \left(\frac{\partial \mathbf{V}}{\partial t} - \frac{D\mathbf{V}}{Dt}\right) + \left(\frac{\rho}{\rho_0} - \frac{\rho'}{\rho_0}\right)\mathbf{g} + \frac{1}{\rho_0 \mu}(\mathbf{B} \cdot \nabla \mathbf{B} - \bar{\mathbf{B}} \cdot \nabla \mathbf{b}), \tag{7}$$

where D/Dt is the conventional material derivative defined in terms of the complete velocity field. The first term in (7) (denoted Φ_R) represents the influence of Reynolds stresses

$$\Phi_R = -\mathbf{V} \cdot \nabla \mathbf{V}, \tag{8}$$

whereas the second term describes the buoyancy force due to convective fluctuations in density

$$\Phi_T = \left(\frac{\rho}{\rho_0} - \frac{\rho'}{\rho_0}\right)\mathbf{g}. \tag{9}$$

The final term in (7) represent the influence of magnetic stresses; the leading-order term (relative to the small perturbations) is

$$\Phi_M = \frac{1}{\rho_0 \mu}\bar{\mathbf{B}} \cdot \nabla \bar{\mathbf{B}}. \tag{10}$$

Since inertial effects are expected to be very small in Earth's core (Davidson 2013), we focus on the role of buoyancy and magnetic forces from the underlying convection.

An additional source term emerges from the induction equation for $\mathbf{B}$. Writing the induction equation for $\mathbf{B}$ in terms of the wave equation plus a correction gives

$$\frac{\partial \mathbf{B}}{\partial t} = \bar{\mathbf{B}} \cdot \nabla \mathbf{v} + \eta \nabla^2 \mathbf{B} + \Phi_I, \tag{11}$$

where $\mathbf{v}$ denotes the part of the velocity associated with wave motion. The correction term is

$$\Phi_I = \left(\frac{\partial \mathbf{B}}{\partial t} - \frac{D\mathbf{B}}{Dt}\right) - \mathbf{B} \cdot \nabla \mathbf{V} - \bar{\mathbf{B}} \cdot \nabla \mathbf{v}, \tag{12}$$

which can be written to leading order as

$$\Phi_I = \nabla \times (\bar{\mathbf{V}} \times \bar{\mathbf{B}}). \tag{13}$$

In summary, we focus on three source mechanisms for MAC waves: buoyancy forces, magnetic (Lorentz) forces and magnetic induction. We subsequently refer to these threes sources as thermal, magnetic and induction mechanisms.

An assumption inherent to the approach of Lighthill (1952) is that the waves do not influence the background flow or magnetic field. There is support for this approximation in the original application to sound waves generated by turbulence (Wang *et al.* 2006). However, it is reasonable to question the assumption in the context of MAC waves. One line of support comes from Lecoanet *et al.* (2015), which uses numerical models to establish the validity of Lighthill's approach for internal waves due to convection in an underlying region (e.g. Stein 1967). Their assessment of Lighthill's approach was based on a comparison of its predictions with fully coupled solutions for convection and wave generation. A similar test of MAC waves is not feasible because these waves are over damped at the conditions accessible to dynamo models. Instead we appeal to the notion that waves in a thin layer at the top of the core have only a small influence on the deeper dynamics when the wave motion is small compared to the interior flow. Current estimates suggest that the wave motion is about 10 per cent of the large-scale convective flow (Buffett 2014).

Downloaded from https://academic.oup.com/gji/article-abstract/212/3/1523/4628047
by University of California, Berkeley/LBL user
on 19 January 2018

2.1 Nearly geostrophic MAC waves

Planetary waves in a relatively thin layer ensure that radial motion is small compared with the horizontal motion (e.g. Pedlosky 1987). Weak radial accelerations imply a nearly hydrostatic balance. In addition, we can discard the horizontal component of the rotation vector in the Coriolis force. The resulting horizontal motion is described to a first approximation by a geostrophic balance between the meridional pressure gradient, $r^{-1}\partial_\theta P$, and the Coriolis force associated with azimuthal flow (denoted v_ϕ). There is no pressure gradient in the ϕ direction for zonal waves, so the Coriolis force associated with meridional flow, v_θ, is balanced by magnetic forces. Writing these force balances in spherical coordinates (r, θ, ϕ) gives (Braginsky 1993)

$$g(\rho'/\rho_0) + \frac{1}{\rho_0}\frac{\partial P}{\partial r} = \hat{\mathbf{r}}\cdot(\Phi_T + \Phi_M) \tag{14}$$

$$2\Omega\cos\theta\, v_\phi - \frac{1}{\rho_0 r}\frac{\partial P}{\partial \theta} = -\hat{\theta}\cdot\Phi_M \tag{15}$$

$$2\Omega\cos\theta\, v_\theta - \frac{B_r}{\rho_0\mu}\frac{\partial b_\phi}{\partial r} = \hat{\phi}\cdot\Phi_M, \tag{16}$$

where we tentatively retain all components of the thermal Φ_T and magnetic Φ_M sources as forcing terms. The form of the Lorentz force on the left-hand side of (16) relies on the fact that radial gradients in the perturbations are large compared with horizontal gradients and with gradients in the background field. In fact, we will subsequently assume that B_r does not vary across the layer, so that $B_r\partial_r b_r$ in (16) can be replaced with $\partial_r(B_r b_r)$; this permits simplifications in the derivation of a wave equation.

Numerical dynamo models show that $\hat{\phi}\cdot\Phi_M$ is the largest component of the magnetic forcing term. It also causes the largest disturbance to the fluid layer because the hydrostatic and geostrophic balances in (14) and (15) dominate the dynamics and are much less affected by the addition of $\hat{r}\cdot\Phi_M$ and $\hat{\theta}\cdot\Phi_M$ (Jaupart & Buffett 2017). Consequently, we limit our attention to $f_M \equiv \hat{\phi}\cdot\Phi_M$ and write the thermal source as $f_T \equiv \hat{\mathbf{r}}\cdot\Phi_T = \alpha_T\delta\bar{T}g$, where $\delta\bar{T}$ is the temperature anomaly due to convection and α_T is the coefficient of thermal expansion. For convection driven by compositional anomalies, $\delta\bar{C}$, we would replace $\alpha_T\delta\bar{T}$ with $\alpha_C\delta\bar{C}$, where α_C is the coefficient of expansion for composition.

Wave motion is most conveniently expressed in terms of the time dependence of the magnetic perturbation b_ϕ. This component of the perturbation is governed by

$$\frac{\partial b_\phi}{\partial t} - \eta\frac{\partial^2 b_\phi}{\partial r^2} - B_r\frac{\partial v_\phi}{\partial r} = \hat{\phi}\cdot\Phi_I \tag{17}$$

where Φ_I is the induction source associated with the background magnetic field. For the sake of consistency of notation we let $f_I \equiv \hat{\phi}\cdot\Phi_I$. A scalar wave equation for b_ϕ is derived by expressing v_ϕ in terms of the magnetic perturbation in (17). The original treatment by Braginsky (1993) was restricted to a dipolar background magnetic field, but the approach can be extended to more general background fields. We defer the details to Appendix A and give the final form of the wave equation for b_ϕ, including the forcing terms due to convection in the core. From Appendix A we have

$$\frac{\partial^2 b_\phi}{\partial t^2} - \eta\frac{\partial^3 b_\phi}{\partial r^2\partial t} - \left(\frac{B_r N^2}{4\Omega^2 R^2}\right)\mathcal{L}_\theta^2\left(\frac{B_r b_\phi}{\rho_0\mu}\right) = S_T + S_M + S_I \tag{18}$$

where the operator $\mathcal{L}_\theta^2$ is defined by

$$\mathcal{L}_\theta^2(\cdot) = \frac{1}{\cos\theta}\frac{\partial}{\partial\theta}\left(\frac{1}{\sin\theta}\frac{\partial}{\partial\theta}\left(\frac{\sin\theta\,(\cdot)}{\cos\theta}\right)\right) \tag{19}$$

and the source terms are

$$S_T = \left(\frac{B_r g\alpha_T}{2\Omega R}\right)\frac{1}{\cos\theta}\frac{\partial^2(\delta\bar{T})}{\partial\theta\partial t} \approx -\left(\frac{B_r g\alpha_T}{2\Omega R}\right)\frac{1}{\cos\theta}\frac{\partial}{\partial\theta}(\bar{\mathbf{V}}\cdot\nabla\bar{T}) \tag{20}$$

$$S_M = \left(\frac{Br N^2}{4\Omega^2 R^2}\right)\mathcal{L}_\theta^2 F_M \tag{21}$$

$$S_I = \frac{\partial}{\partial t}(\nabla\times\bar{\mathbf{V}}\times\bar{\mathbf{B}})\cdot\hat{\phi}. \tag{22}$$

The effects of thermal diffusion have been dropped in (20) because of the long wavelengths and relatively short periods. The buoyancy frequency, N, in (18) is defined by

$$N = \sqrt{-\frac{g}{\bar{\rho}}\frac{\partial\bar{\rho}}{\partial r}} \tag{23}$$

and the quantity F_M in the definition of the magnetic source in (21) is related to f_M by

$$F_M(r,\theta) = \int_R^r f_M(r',\theta)\,\mathrm{d}r'. \tag{24}$$

(see Appendix A for details). The wave equation in (18) and the sources in (20)–(22) are the main focus of this study. We use a dynamo model to characterize the source terms and we integrate the wave equation numerically using these sources to quantify the amplitude of MAC waves at the surface of the core.

2.2 Numerical solution for MAC waves

Solutions to (18) are obtained numerically using the finite difference method. A thin layer at the top of the core is discretized with an evenly spaced grid in r and $x = \cos\theta$. (The choice of x rather than θ permits some simplifications in the discretization of $\mathcal{L}_\theta^2$.) The time dependence is eliminated from the problem by taking the Fourier transform of (18). We define the Fourier transform by

$$\tilde{b}_\phi(f,r,x) = \int_{-\infty}^{\infty} b_\phi(t,r,x)e^{-2\pi i f t}\,\mathrm{d}t, \tag{25}$$

where f is the frequency in cycles per unit time. The Fourier transform of the wave equation becomes

$$-4\pi^2 f^2\tilde{b}_\phi - 2\pi i f\eta\frac{\partial^2\tilde{b}_\phi}{\partial r^2} - \frac{Br N^2}{4\Omega^2 R^2}\mathcal{L}_x^2\left(\frac{B_r\tilde{b}_\phi}{\rho_0\mu}\right) = \tilde{S}_T + \tilde{S}_M + \tilde{S}_I, \tag{26}$$

where

$$\mathcal{L}_x^2(\cdot) = \frac{\sqrt{1-x^2}}{x}\frac{\partial^2}{\partial x^2}\left(\frac{\sqrt{1-x^2}}{x}(\cdot)\right). \tag{27}$$

Derivatives in both x and r are evaluated to second-order accuracy using central differences.

Solutions for $\tilde{b}_\phi(f,r,x)$ are subject to boundary conditions at the top and bottom of the layer. We expect $\tilde{b}_\phi$ to vanish at the interface with the insulating mantle ($r = R$). We also expect $\tilde{b}_\phi$ to vanish below the magnetic skin depth at the base of the layer. We account for the skin depth in the solution by retaining a small region of neutral stratification below the layer. Setting $N^2 = 0$ below the layer in the absence of forcing yields

$$\eta\frac{\partial^2\tilde{b}_\phi}{\partial r^2} = 2\pi i f\,\tilde{b}_\phi \tag{28}$$

Downloaded from https://academic.oup.com/gji/article-abstract/212/3/1523/4628047
by University of California, Berkeley/LBL user
on 19 January 2018

which admits solutions

$$\tilde{b}_\phi(r) = \tilde{b}_\phi(R_b) e^{\pm(1+i)(r-R_b)/\delta} \tag{29}$$

where $b_\phi(R_b)$ is the magnetic perturbation at the base of the stratified layer ($r = R_b$) and

$$\delta = \sqrt{\frac{\eta}{\pi f}}, \tag{30}$$

defines the skin depth. Consequently, we include a region of neutral stratification below the layer with a thickness of several δ, based on the nominal wave frequency, and set $\tilde{b}_\phi = 0$ at the base of this expanded domain. We also impose $\tilde{b}_\phi = 0$ at the poles ($x = \pm 1$) by incorporating these conditions into the discretization of $\mathcal{L}_x^2$.

The discrete form of the unforced wave equation (i.e. $\tilde{S} = 0$) can be written as a standard eigenvalue problem for an expanded solution vector $\mathbf{y}(t) = [b_\phi, \partial_t b_\phi]^T$. In effect, a second-order differential equation for b_ϕ is converted into two first-order equations for b_ϕ and $\partial_t b_\phi$. The eigenvalue problem for the waves becomes

$$(\mathbf{A} - 2\pi i f \mathbf{I}_n)\,\tilde{\mathbf{y}} = 0, \tag{31}$$

where $\mathbf{I}_n$ is an identify matrix of size $n \times n$ (where n is the length of $\tilde{\mathbf{y}}$) and $\mathbf{A}$ has the structure

$$\mathbf{A} = \begin{bmatrix} 0 & \mathbf{I}_{n/2} \\ \mathbf{D}_x^2 & \mathbf{D}_r^2 \end{bmatrix}. \tag{32}$$

Here $\mathbf{D}_x^2$ represents the discretization of $\mathcal{L}_x^2$ and $\mathbf{D}_r^2$ defines the second-order derivative in r. Solutions for the waves are validated using both analytical (Braginsky 1993) and numerical (Buffett *et al.* 2016) solutions. Wave frequencies for the case of a dipolar background magnetic field converge toward the analytical (diffusion-free) solutions of Braginsky (1993) when the effects of magnetic diffusion are reduced. Lowering η by a factor of four in the numerical calculations from our preferred value of $\eta = 0.8$ m^2 s^{-1} (Pozzo *et al.* 2012; Gomi *et al.* 2016) reproduces the analytical solution to within 0.1 per cent. Numerical convergence is achieved with a resolution of 80 × 80 grid points in the x and r coordinates. (The radial resolution is set by the need to resolve the magnetic skin depth.) We also reproduce the numerical solution of Buffett *et al.* (2016) to within 1 per cent for the case of a constant background field. These results are notable because the previous numerical solution retained a full description of the dynamics, including the effects of local inertia, the horizontal component of the rotation vector, as well as the θ component of the magnetic induction and the associated Lorentz force in the momentum equation. Good agreement with the current solution means that the approximations introduced in Section 2.1 are reasonable.

Generation of MAC waves with an imposed source can be represented by

$$(\mathbf{A} - 2\pi i f \mathbf{I})\,\tilde{\mathbf{y}} = \tilde{S}, \tag{33}$$

where $\tilde{S} = [0, \tilde{S}_k]^T$ and $\tilde{S}_k$ represents one or more of the various source terms in the Fourier domain. Each $\tilde{S}_k(f, r, x)$ has a known spatial form. For example, the dynamo model gives estimates for the x dependence in terms of Legendre functions $P_l^m(x)$. Similarly, the radial dependence of all source terms in the dynamo model is found to decrease across the layer and vanishes at the core–mantle boundary (CMB; $r = R$). For our purposes it suffices to adopt a linear dependence in r, although we revisit this assumption in Section 5. The frequency dependence is computed by taking a Fourier transform of the time-dependent output of the dynamo model. Thus we define the time dependence of the source using $S_k(t, r, x) = s_k(r, x)h_k(t)$ and compute the Fourier transform as $\tilde{S}_k(f, r, x) = s_k(r, x)\tilde{h}(f)$. Setting $\tilde{h}(f) = 1$ for the source in (33) defines a Green's function, $\tilde{\mathbf{G}}_k(f, r, x)$, for the response to a source with a specified spatial distribution (e.g. $s_k(r, x)$). A general time-dependent response is obtained by convolution or by multiplication in the Fourier domain. Consequently, the jth component of the solution vector $\tilde{\mathbf{y}}$ is written as

$$\tilde{y}_j = \tilde{G}_j \tilde{h}, \tag{34}$$

where we use $\tilde{G}_j = (\tilde{\mathbf{G}}_k)_j$ to simplify notation. It follows that

$$\tilde{y}_j \tilde{y}_j^* = \tilde{G}_j \tilde{G}_j^* (\tilde{h}\tilde{h}^*). \tag{35}$$

For a long time series, the power spectrum of $h(t)$ is approximated by

$$P_{hh} \approx \frac{\tilde{h}\tilde{h}^*}{T}, \tag{36}$$

where T is the duration of the record. As a result the power spectrum for an individual element of the response is given by (Rice 1954)

$$P_{yy} \approx \tilde{G}_j \tilde{G}_j^* P_{hh}. \tag{37}$$

In other words, we arrive at a statistical description of the response in terms of the statistical description of the source. When other quantities of interest (like $\tilde{v}_\phi$) are linearly related to $\tilde{\mathbf{y}}$ by

$$\tilde{z}_i = C_{ij}\tilde{y}_j = C_{ij}\tilde{G}_j\tilde{h}, \tag{38}$$

we compute the associated power spectrum using

$$P_{zz} = C_{ij}C_{ik}^* G_j G_k^* P_{hh}. \tag{39}$$

We now seek an estimate for P_{hh} using the output of a dynamo model.

3 ESTIMATION OF SOURCE TERMS

3.1 Numerical dynamo model

We use the dynamo model *Calypso* (Matsui *et al.* 2014) to evaluate the source terms in (20)–(22). The model setup includes a uniform heat sink in the temperature equation to represent the influence of conduction down the adiabatic gradient (e.g. Olson *et al.* 2017). Stable stratification develops at the top of the core when the volume-integrated heat sink exceeds the heat flow through the lower (inner-core) boundary (at $r = R_i$). This setup is intended to approximate the effects of a subadiabatic temperature gradient at the CMB (Gubbins *et al.* 1982).

The governing equations are written in non-dimensional form using the diffusion-free scales of Christensen & Aubert (2006). We adopt the thickness of the fluid shell $L = R - R_i$ as a characteristic length scale and Ω^{-1} as the characteristic timescale. Velocity is scaled by ΩL, the magnetic field is scaled by $\sqrt{\rho\mu}\Omega L$, and temperature is scaled by the fixed temperature difference ΔT between the top and bottom boundaries. Solutions are specified by the amplitude of the heat sink Q and by four additional dimensionless parameters:

$$E = \frac{\nu}{\Omega L^2}, \quad Pr = \frac{\nu}{\kappa}, \quad Pm = \frac{\nu}{\eta}, \quad Ra^* = \frac{\alpha_T g(R)\Delta T}{\Omega^2 L} \tag{40}$$

which include the Ekman number, E, the Prandtl number, Pr, the magnetic Prandtl number, Pm, and a modified Rayleigh number, Ra^*. Here α_T is the coefficient of thermal expansion, $g(R)$ is the gravitational acceleration at the CMB, ν is the viscosity and κ is the thermal diffusivity. Both the mantle and inner core ($r < R_i$)

Downloaded from https://academic.oup.com/gji/article-abstract/212/3/1523/4628047
by University of California, Berkeley/LBL user
on 19 January 2018

Table 1. Numerical solutions used in study.

#	E	Pm	Pr	Ra^*	Q	Rm	Λ	$N(\Omega)$	Source
1	5×10^{-5}	0.45	1	0.070	-3.0×10^{-4}	84	0.69	0.20	This study
2	10^{-5}	0.20	1	0.032	-1.2×10^{-4}	105	0.43	0.14	This study
3	10^{-5}	0.50	1	0.032	-1.2×10^{-4}	236	1.89	0.14	This study
4	10^{-5}	0.50	1	0.035	0	228	4.37	0	C&A2006
5	10^{-5}	1.44	1	0.070	0	970	31.0	0	A+2017

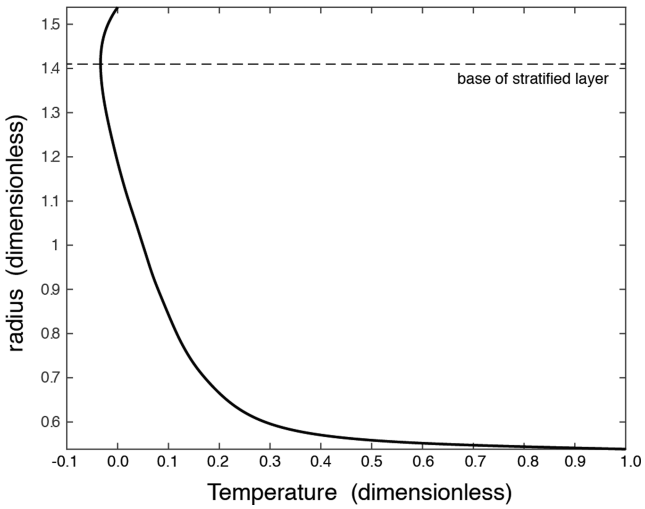

Figure 1. Time-averaged radial temperature profile from *Calypso* dynamo model (Solution 2). A region of stable stratification develops at the top of the core when the volume-integrated heat sink in the temperature equation exceeds the heat flow across the lower boundary.

are assumed to be electrically insulating. An Earth-like geometry is adopted by setting $r = 1.5385$ and $r = 0.5385$ for the dimensionless radius of the core-mantle and inner-core boundaries.

The source terms are evaluated using several different numerical solutions (see Table 1). The bulk of the results are computed using Solution 2 from Table 1. We also consider a lower resolution solution (higher E) to assess the influence of changing control parameters away from Earth-like conditions. We also include a third solution (#3 in Table 1) to illustrate the dependence on Pm. Two important diagnostics of the solutions include the magnetic Reynolds number,

$$Rm = \frac{V_{\rm rms} L}{\eta}, \tag{41}$$

and the Elsasser number

$$\Lambda = \frac{B_{\rm rms}^2}{\rho \mu \Omega \eta}, \tag{42}$$

which characterize, respectively, the vigor of convection and the strength of the magnetic field. We also define a dimensionless strength of stratification in the layer using N/Ω. Numerical solutions without a stratified layer are assign a value $N/\Omega = 0$.

A uniform heat source of $Q = -1.2 \times 10^{-4}$ in our main numerical solution corresponds to a dimensionless volume-integrated heat sink of -0.0018. By comparison, the time-averaged heat flow across the lower boundary is $q = -4\pi R_i^2 E Pr^{-1} {\rm d}T/{\rm d}r = 0.0016$. The imbalance causes a heat flow into the top of the core to satisfy the time-averaged the energy budget. A positive radial temperature gradient develops at the CMB, producing a thin region of stable stratification (see Fig. 1).

The dimensionless temperature gradient at the CMB for Solution 2 is ${\rm d}T/{\rm d}r = 0.62$, which corresponds to a dimensionless stratification $N/\Omega = \sqrt{Ra^* \, dT/dr} = 0.14$. Values for the other solutions are listed in Table 1. These values are roughly four to six times smaller than the value $N/\Omega = 0.84$ proposed by Buffett *et al.* (2016). On the other hand, the thickness of the layer is greater than the preferred estimate of 140 km by roughly a factor of two. For example, the time-averaged temperatures in Solutions 2 and 3 reach a minimum value at $r = 1.41$, corresponding to a region of stable stratification in the top 290 km of the core. Increasing the heat sink would strengthen the stratification, but it would also increase the layer thickness. Our choice of model parameters represents a compromise for the properties of the stable layer. The consequences of stronger stratification (relevant for more Earth-like conditions) are examined in Section 5.

Fig. 2(a) shows buoyant fluid rising from the inner-core boundary and penetrating into the region of stable stratification. These anomalies account for the generation of MAC waves due to the thermal source. We also find Lorentz forces permeating into the stratified layer from the interior of the core (see Fig. 2b). These forces tend to be symmetric about the equator, although the value on the equator nearly vanishes. In general, the Lorentz forces are weaker toward the outer boundary, but they still contribute significantly to the generation of MAC waves, and may even dominant the generation process when these sources are extrapolated to Earth-like conditions.

The role of thermal stratification on the generation of magnetic field is revealed by comparing our higher Pm solution (#3) with a very similar solution from Christensen & Aubert (2006) (#4). These solutions have identical E and Pm and similar values for Ra^* and Rm. Larger differences are evident in Λ. Including a heat sink in solution #3 lowers the value of Λ by more than a factor of two. Thus the style of convection can have an important influence on both the magnetic field and the magnetic source for MAC-wave generation. Stratification is also expected to reduce the complexity of the radial magnetic field at the core mantle boundary (e.g. Jaupart & Buffett 2017).

3.2 Time dependence of sources

MAC waves are not directly detected in the dynamo model because the accessible parameters causes excessive damping of the waves. However, we can evaluate the source terms using the expressions given in (20)–(22). We begin with the case of thermal forcing due to S_T. Fig. 3(a) shows the $l = 2$ and $m = 0$ part of $-\bar{\mathbf{V}}' \cdot \nabla' \bar{T}'$ as a function of time in the vicinity of the stratified layer. (Here we use primes to indicate dimensionless fields from the dynamo model; recall that the bar over $\mathbf{V}$ or T denotes a background field.) Positive and negative temperature fluctuations are largest below the stratified layer, although many of these fluctuations extend up into the stratified region. The largest fluctuations begin with a warming phase (positive source) as hot, buoyant parcels rise into the boundary region. Warming is followed by cooling (negative source) as the warm parcels pass through the region and the temperature returns to the time-averaged value.

Downloaded from https://academic.oup.com/gji/article-abstract/212/3/1523/4628047
by University of California, Berkeley/LBL user
on 19 January 2018

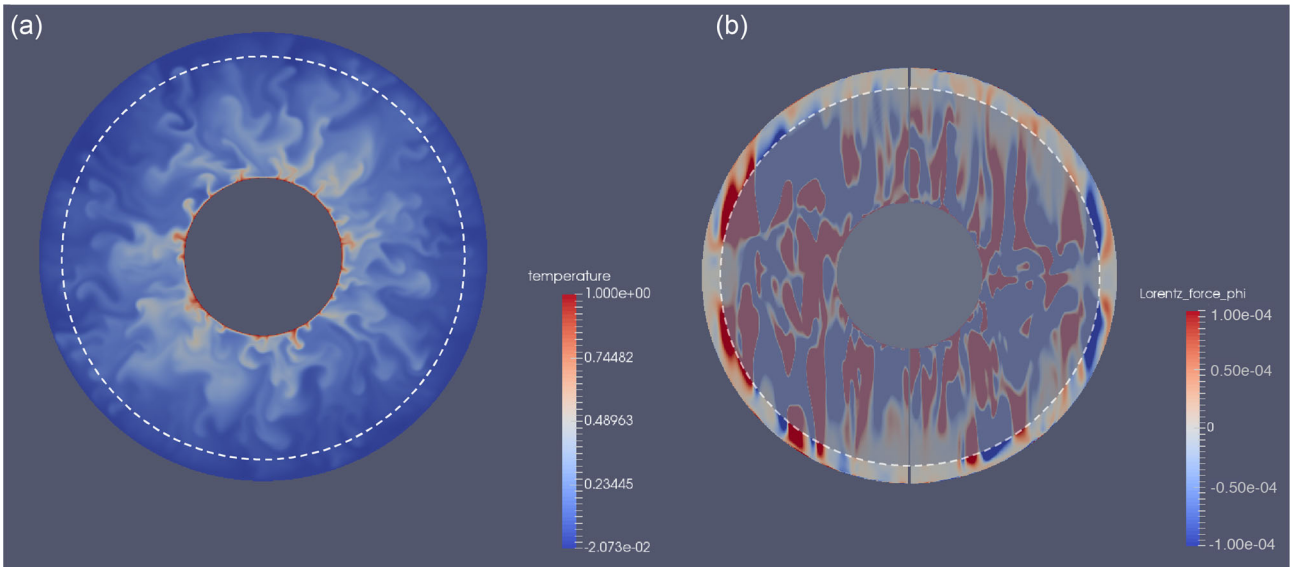

Figure 2. (a) Snapshot of temperature in the equatorial plane from Solution 2. Warm plumes rise from the inner-core boundary and penetrate into base of stratified layer (dashed line). (b) Snapshot of ϕ component of Lorentz force, f_ϕ, in a meridional plane. The colour scale is saturated in the interior of the core to emphasize the structure of f_ϕ in the stratified layer. An opaque mask covers the convecting region of the core.

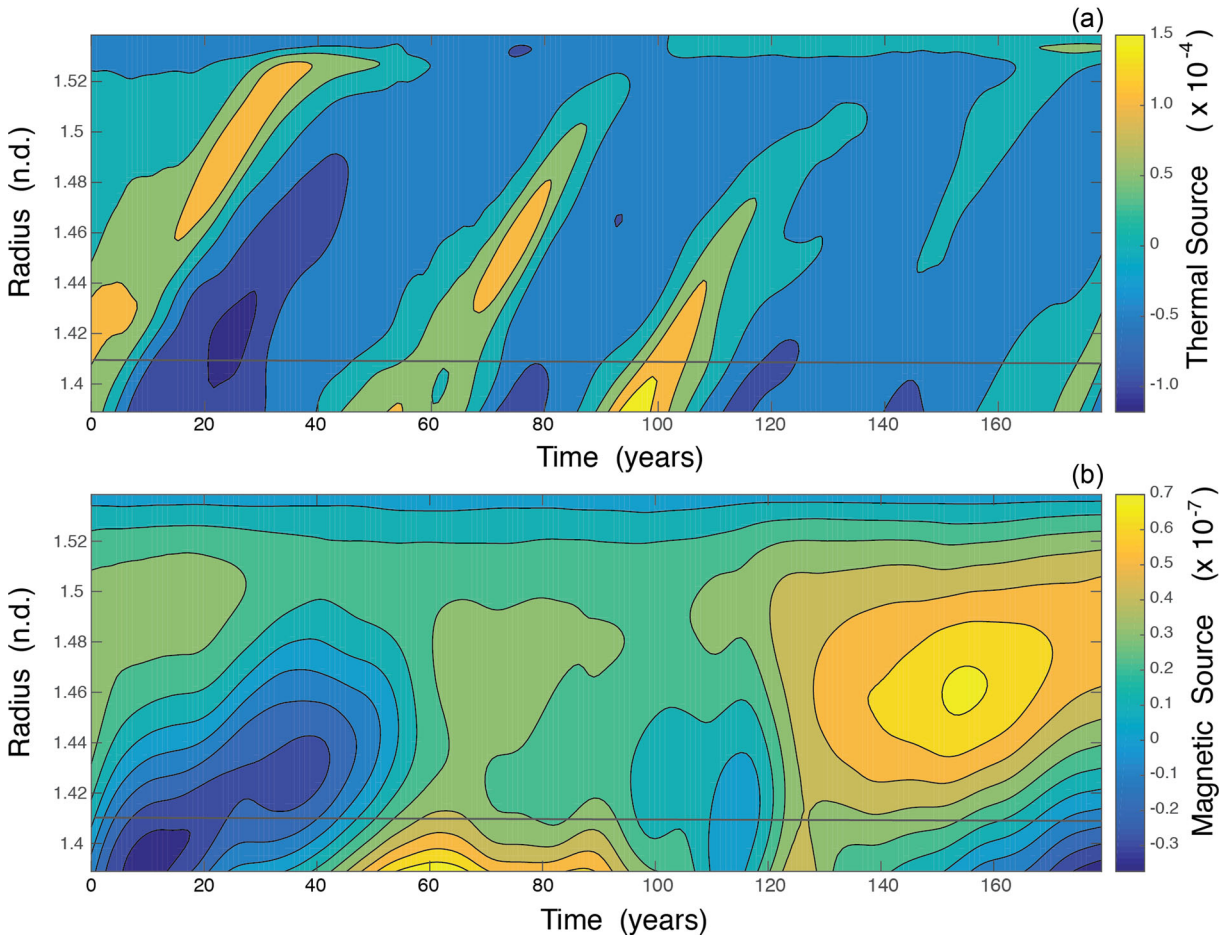

Figure 3. (a) Thermal fluctuations due to degree 2 part of $-\mathbf{V} \cdot \nabla \mathbf{T}$ in the vicinity of the stratified layer. Positive (negative) sources corresponds to warming (cooling). (b) Magnetic fluctuations due to degree 3 part of F_M reveal low frequency fluctuations inside the stratified layer. Both of these fluctuations contribute to the generation of MAC waves.

Downloaded from https://academic.oup.com/gji/article-abstract/212/3/1523/4628047
by University of California, Berkeley/LBL user
on 19 January 2018

The source due to the Lorentz force is shown in Fig. 3(b). We specifically show the $l = 3$ and $m = 0$ part of F_M, which was defined in (24) as the radially integrated Lorentz force. The dimensionless Lorentz force in the dynamo model is

$$f'_M(r, x) = \hat{\phi} \cdot (\bar{\mathbf{B}}' \cdot \nabla' \bar{\mathbf{B}}') \tag{43}$$

so

$$F'_M(r, x) = \int_R^r f'_M(\mathrm{r}, x)\, \mathrm{dr}. \tag{44}$$

We focus on the $l = 3$ part of f'_M and F'_M because $\mathcal{L}_x^2 F'_M$ contributes most to the $l = 2$ MAC wave (see Appendix B). This makes the outcome directly comparable to the thermal forcing at $l = 2$. However, the relative magnitudes of F'_M and $-\bar{\mathbf{V}}' \cdot \nabla' \bar{T}'$ do not fully convey the importance of these sources for wave generation because we need to include the pre-factors in the definitions of S_M and S_T from (20) and (21). For example, the pre-factor for the magnetic source, S_M, depends on the strength of stratification, whereas the pre-factor for S_T does not. This does not mean the effects of stratification are unimportant for the thermal source. Penetration of convective anomalies into the stratified layer depends strongly on the strength of stratification and this will have a substantial influence on the efficiency of the thermal source. Because we consider a range of parameter values for N and $\bar{B}_r$, we treat the pre-factors separately. Nevertheless, qualitative differences in the time dependence of the two sources are evident in Fig. 3, which will affect the frequency of waves that are generated.

Dimensionless time in the dynamo model is converted to years by making a particular choice for the rotation rate, Ω, in the model. Using Earth's rotation rate of $\Omega = 0.729 \times 10^{-4}$ s^{-1} in the numerical calculations gives a root-mean-square (rms) velocity of about 0.037 mm yr^{-1}. This value is about an order of magnitude smaller than the rms velocity, $V_{\mathrm{rms}} = 0.38$ mm s^{-1}, inferred from core-surface flow (Holme 2015). By adjusting the rotation rate in the model to $\Omega = 7.383 \times 10^{-4}$ s^{-1} we produce an rms velocity that matches the core-surface flow. An comparable approach relies on the observed timescale for fluctuations in the potential field outside the core (Lhuillier *et al.* 2011; Christensen *et al.* 2012). It has become customary (e.g. Bouligand *et al.*, 2016) to assume that the secular variation time, τ_{sv}, is about three times the overturn time $\tau_u = L/V_{\mathrm{rms}}$. In this case the adjusted rotation rate gives $\tau_u = 188$ yr and $\tau_{\mathrm{sv}} = 564$ yr, which is not too far from the value $\tau_{\mathrm{sv}} = 415$ yr, inferred from magnetic-field observations by Lhuillier *et al.* (2011). It is not our intent to exactly reproduce the time dependence of the present-day magnetic field. Instead, we seek to adjust the timescale of the source terms relative to the expected wave periods. A separate question concerns the amplitude of those fluctuations (see Section 5).

3.3 Power spectra of sources

Power spectra for the thermal, magnetic and induction sources are shown in Fig. 4 for several spherical harmonic degrees ($l = 2$, 3, 4). Each l defines how the source $s_k(r, x)$ varies with x. Thermal and induction sources with $l = 2$, 3, 4 are primarily responsible for exciting MAC waves at $l = 2$, 3, 4, whereas the magnetic force at a particular l tends to excite waves at a lower degree (e.g. $l' = l - 1$). To facilitate comparisons between the various sources, we report the results in Fig. 4 according to the primary degree of the excited waves. Each source is evaluated at the base of the stratified layer, $r = 1.41$, using dimensionless quantities from the dynamo model. These quantities must be converted to physical dimensions

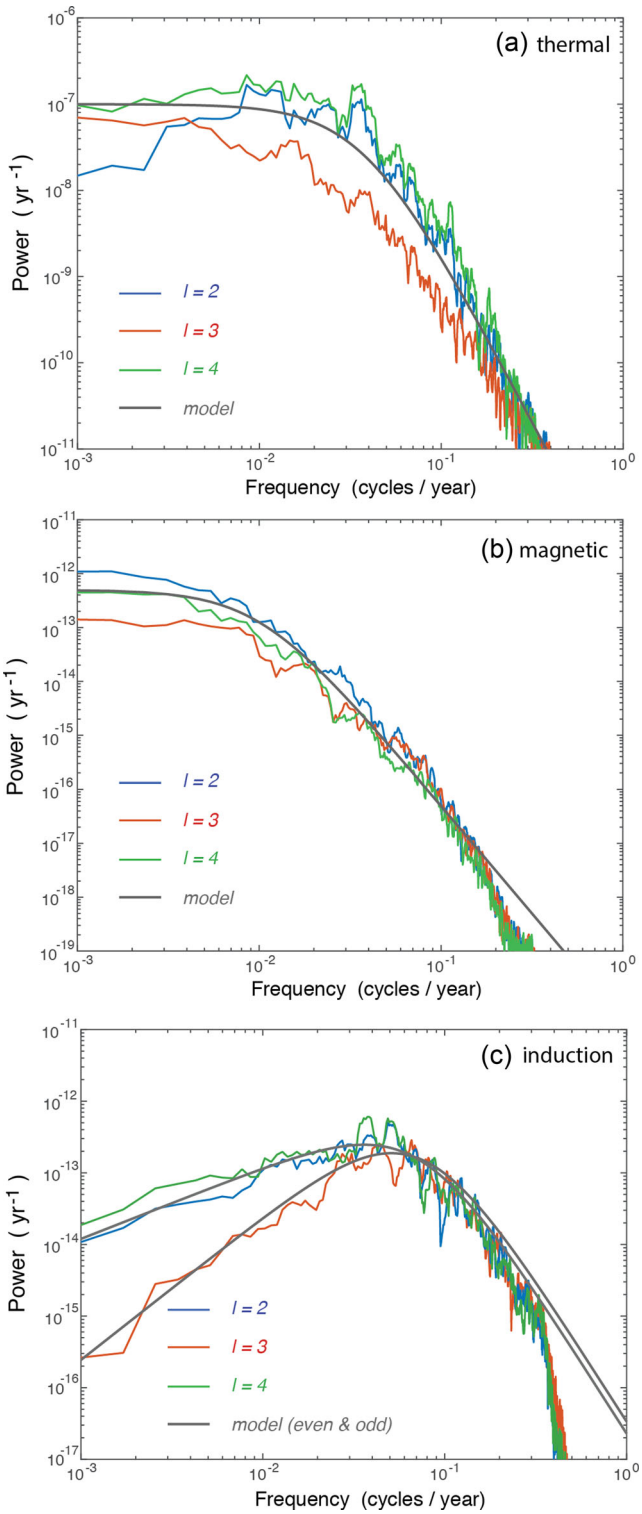

Figure 4. Power spectra for (a) thermal, (b) magnetic and (c) induction sources computed from Solution 2 as a function of frequency (in cycles yr^{-1}). Degrees $l = 2$, 3, 4 refer to the primary degree of the waves generated by these sources. Even degrees represent waves with symmetric v_ϕ about the equator. A parameter fit (model) is based on the nominal corner frequency of the spectra and the standard deviation of the input time-series. A distinction is made between even and odd waves in the induction sources. Discrepancies between the model and computed spectra are not significant outside the frequency range of MAC waves ($f = 0.01$ to 0.1 cycles yr^{-1}).

Downloaded from https://academic.oup.com/gji/article-abstract/212/3/1523/4628047
by University of California, Berkeley/LBL user
on 19 January 2018

to solve the (dimensional) wave equation in (18). Alternatively, we could convert the wave equation to dimensionless form and use the dimensionless sources directly from the dynamo model. Both approaches are equivalent, and we adopt the second approach here. However, for the purposes of presentation it is helpful to tabulate the dimensionless sources from the dynamo model as a function of time in years. The resulting power spectra computed from these time series have units yr^{-1}. Use of dimensionless time instead would simply alter the frequency axis without changing the shape of the power spectra. In either case we recover the variance of the dimensionless sources in the dynamo model by integrating the spectra over the relevant frequency.

Power spectra for the thermal and magnetic sources have broadly similar structure. A useful parametric representation has the general form

$$P_{hh}(f) = \frac{4\alpha^3 \sigma_{hh}^2}{(\alpha^2 + 4\pi^2 f^2)^2} \tag{45}$$

where σ_{hh} defines the standard deviation of the source and α specifies the corner frequency in the spectra. This specific form is chosen to give constant power at low frequency and a f^{-4} decrease at high frequency, similar to the frequency spectrum of Gauss coefficients for the non-dipole field (Bouligand *et al.* 2016). Taking the inverse Fourier transform gives the autocovariance function,

$$C_{hh}(t) = \sigma_{hh}^2 (1 + |\alpha t|) e^{-|\alpha t|}, \tag{46}$$

which shows that α is related to the correlation time. Since the correlation drops by a factor e^{-1} when $|\alpha t| = 2.15$, we define an effective correlation time using $\tau_c = 2.15/\alpha$. The effective correlation times for the thermal and magnetic sources are nominally $\tau_c = 9$ and 34 yr, respectively.

Systematic differences in σ_{hh} are evident for even and odd l. The standard deviations for the thermal source at even degrees are $\sigma_{hh} = 6.3 \times 10^{-5}$ and 7.8×10^{-5}, whereas the odd degree gives $\sigma_{hh} = 3.2 \times 10^{-5}$. Similarly the magnetic source has standard deviations $\sigma_{hh} = 1.0 \times 10^{-7}$ and 0.70×10^{-7} at even degrees, and $\sigma_{hh} = 0.44 \times 10^{-7}$ at the odd degree. Both the thermal and magnetic sources have more power in even degrees, meaning that even degree waves are preferentially generated (Jaupart & Buffett 2017). Such waves are associated with symmetric v_ϕ about the equator. Departures of the odd sources from the model in (45) is not significant because we confine our attention to even waves. Similarly, departures at high frequency are not a concern because we are interested in waves with frequencies between $f = 0.01$ to 0.1 cycles yr^{-1}. Waves at higher frequencies would be difficult to detect at Earth's surface due to their short wavelengths.

The spectrum for the induction source (Fig. 4c) is qualitatively different than either the thermal or magnetic source spectrum. The computed spectra for $l = 2, 3, 4$ suggest a distinct functional form for even and odd l. A useful representation for the even degrees is

$$P_{hh}^e = \frac{6\pi^2 \alpha^3 \sigma_{hh}^2 f}{(\alpha^2 + 4\pi^2 f^2)^{5/2}}, \tag{47}$$

while the odd degree is described by

$$P_{hh}^o = \frac{64\pi^2 \alpha^3 \sigma_{hh}^2 f^2}{(\alpha^2 + 4\pi^2 f^2)^3}. \tag{48}$$

Both spectra share a common corner frequency, $\alpha = 0.45\ \mathrm{yr}^{-1}$, corresponding to an effective correlation time $\tau_c = 2.15/\alpha = 4.8$ yr, although we note that the covariance functions associated with (47) and (48) are not the same as that given in (46). Nevertheless, the induction source produces higher frequency fluctuations than either of the other two sources. Standard deviations for the induction source are not too different for even and odd l. Even degrees are slightly larger with $\sigma_{hh} = 2.1 \times 10^{-7}$ and 2.2×10^{-7} versus $\sigma_{hh} = 1.9 \times 10^{-7}$ for the odd degree. However, spectra over the relevant frequencies for MAC waves ($f \approx 0.01$ to 0.1 yr^{-1}) are nearly equal. This suggests that even and odd waves should be excited equally by this mechanism.

4 STOCHASTIC FORCING OF MAC WAVES

What do the power spectra tell us about the amplitude of the generated waves? To answer this question we must first to relate the dimensionless source terms from the dynamo model to the physical quantities that appear in the wave equation in (18). It is convenient to write the wave equation in dimensionless form using the characteristic scales from the dynamo model. The resulting wave equation becomes

$$\frac{\partial^2 b'_\phi}{\partial t^2} - E_\eta \frac{\partial^3 b'_\phi}{\partial r^2 \partial t} - \frac{1}{4} \bar{B}'_r N'^2 \left(\frac{L}{R}\right)^2 \mathcal{L}_x^2 \left(\bar{B}'_r b'_\phi\right) = \frac{1}{\Omega^2 \mathcal{B}} (S_T + S_M + S_I) \tag{49}$$

where $N'^2 = N^2/\Omega^2$ is the dimensionless buoyancy frequency and

$$E_\eta = \frac{\eta}{\Omega L^2} \tag{50}$$

is the magnetic Ekman number. It is important to note that E_η is evaluated for the waves using realistic physical properties. Taking $\eta = 0.8\ \mathrm{m^2\ s^{-1}}$, $L = 2.259 \times 10^6$ m and $\Omega = 0.729 \times 10^{-4}$ gives $E_\eta = 2.15 \times 10^{-9}$. On the other hand, the sources S_T, S_M and S_M on the right-hand side of (49) have been evaluated from a dynamo model with unrealistic parameters. This difference will affect the way that we interpret the resulting wave amplitude.

Source terms S_T, S_M and S_I in (49) are still expressed in their dimensional form (with units $\mathrm{T\ s^{-2}}$), although the factor $\Omega^2 \mathcal{B}$ makes the overall equation dimensionless. Consequently, our final step is to express the sources in terms of dimensionless quantities from the dynamo model. For example, the dimensional temperature fluctuation in the definition of S_T can be written as

$$\bar{V} \cdot \nabla \bar{T} = \Omega \Delta T (\bar{V}' \cdot \nabla' \bar{T}'). \tag{51}$$

Substituting (51) into S_T from (20) gives

$$\frac{S_T}{\Omega \mathcal{B}} = \frac{1}{2} \bar{B}'_r Ra^* \left(\frac{L}{R}\right) \frac{\sqrt{1-x^2}}{x} \frac{\partial}{\partial x} (\bar{\mathbf{V}}' \cdot \nabla' \bar{T}') \tag{52}$$

which defines the thermal source for the dimensionless wave equation. The other dimensionless sources are

$$\frac{S_M}{\Omega^2 \mathcal{B}} = \frac{1}{4} \bar{B}'_r N'^2 \mathcal{L}_x^2 F'_M, \tag{53}$$

$$\frac{S_I}{\Omega^2 \mathcal{B}} = \frac{\partial}{\partial t'} \left[\nabla' \times (\bar{\mathbf{V}}' \times \bar{\mathbf{B}}')\right] \cdot \hat{\phi}. \tag{54}$$

Power spectra from the previous section characterize the fluctuations in these dimensionless sources. The sources also depend on $\bar{B}'_r$ and N', which are treated as adjustable parameters. Two specific cases are considered. In one case $\bar{B}'_r$ is assumed to be a dipole and N' is constant across the layer. In the other case we take $\bar{B}'_r$ to be constant over the surface of the core and allow N' to vary linearly across the layer with a maximum value at the CMB. Numerical solutions for the waves are first obtained using $P_{hh} = 1$ (e.g. $\tilde{h} = 1$) and the resulting power spectrum for the waves is multiplied by the

Downloaded from https://academic.oup.com/gji/article-abstract/212/3/1523/4628047
by University of California, Berkeley/LBL user
on 19 January 2018

power spectrum of the source from the dynamo model to define the wave amplitude. A solution for v_ϕ is computed from the induction equation for b_ϕ by integrating $\partial_r(\bar{B}_r v_\phi)$ over radius assuming that the velocity vanishes at the base of the extended domain (i.e. including a narrow region below the stratified layer).

Fig. 5 shows the power spectra for v_ϕ at the top of the core in $m^2\ s^{-2}\ yr^{-1}$. Striking differences are found for solutions with a dipolar $\bar{B}_r$ and constant N (column 1) versus a constant $\bar{B}_r$ and a linearly varying N (column 2). Consider the solutions for the thermal source in the first row of Fig. 5. The thermal source for a dipolar field, $\bar{B}_r(x) = B_d\, x$, can be represented by a single Legendre function $P_l^1(x)$. Similarly, the spatial structure of the wave is described by a single Legendre function (also $P_l^1(x)$). Orthogonality of Legendre functions means that the source at a given l produces a single peak in the response. The quality factor of these waves increases with l, so the amplitude of the response initially increases. However, at high l (and f) the power in the source decreases and the amplitude of the response decreases accordingly.

The response to thermal forcing in a layer with linearly varying N and a constant $\bar{B}_r$ (column 2) is different for two reasons. First, the waves and the forcing are no longer represented by a single Legendre function. As a result, thermal forcing at a single l (corresponding to the degree of $\bar{\mathbf{V}}' \cdot \nabla' \bar{T}'$) excites waves with a range of spatial patterns. Second, the radial overtones have different frequencies and quality factors. By contrast, the overtones in a layer with constant N have the same frequency. This additional complexity in the structure of the overtones produces a more broadly distributed response.

Magnetic forcing exhibits some important differences from thermal forcing. The spatial structure of the magnetic source is specified by $\mathcal{L}_x^2 F_M'$, which is not characterized by a single Legendre function (see Appendix B). Even though the waves for a dipolar $\bar{B}_r$ are still represented by a single $P_l^1(x)$, the complexity of the source produces several peaks for a single l in the source term. Moreover, the amplitude of $\mathcal{L}_x^2 F_M'$ increases roughly as $l(l+1)$, which is reflected in the response at larger l. Eventually, the response at high l and f decreases because the power in the source drops off sharply with frequency. A diffuse response is predicted for a constant $\bar{B}_r$ and linearly varying N, as before, but the largest response is predicted at the largest l.

Magnetic induction produces a response that is broadly similar to thermal forcing, although the power spectrum for induction source increases with frequency below about 0.04 cycles yr^{-1}. This explains the increase in the response with f and l. For the case of a layer with linearly varying N and constant B_r, we continue to see similarities with thermal forcing, but the response at higher l is more prominent because of the shape of the power spectrum for this source.

Integrating the power spectra for v_ϕ over frequency determines the mean square velocity at the top of the core. We focus on a layer with linearly varying N and constant $\bar{B}_r$ because this case has previously been used to explain historical variations in the magnetic field (Buffett *et al.* 2016). The amplitude of waves inferred from the observations is a few km yr^{-1} or about 3×10^{-5} m s^{-1}. By comparison, the thermal, magnetic and induction sources produce wave velocities of 0.34, 0.075 and 5.7 m s^{-1}, respectively, when contributions from $l = 2$ to 10 are included. These values are substantially larger than those inferred from observations. These velocities are also much larger than those recovered from the dynamo model. Neither of these results is very surprising. We used a realistic value for $E_\eta = 2.15 \times 10^{-9}$ in the wave equation, whereas the value in the dynamo model is $E_\eta = E/Pm = 5 \times 10^{-5}$. Adopting the value from the dynamo model in the wave equation would cause heavy damping of the waves and reduce the wave amplitudes. We also note that the fields from the dynamo model greatly exceed the expected values at core conditions. For example, the dimensionless velocity can be interpreted as a Rossby number, $V/\Omega L \approx 5 \times 10^{-3}$, which would be much lower at realistic conditions. Similar arguments apply to $\bar{T}'$ and $\bar{\mathbf{B}}'$. Consequently, the sources computed from these fields are substantially overestimated relative to values expected in the core. We now turn to the question of what the sources would be if we could run the dynamo models at realistic conditions.

5 EXTRAPOLATION OF PREDICTIONS TO CONDITIONS IN THE CORE

General trends in the amplitude of the source terms can be assessed using the results of other dynamo solutions. For example, Solution 1 has higher values for E, Pm and Ra^*, all consistent with less Earth-like conditions. The source terms from this solution are systematically higher than those from Solution 2 by nearly a factor of five. In detail, the ratios of thermal, magnetic and induction sources are 4.80, 4.88 and 4.75, respectively. This result implies that shifting the model parameters in the other direction toward Earth-like conditions would produce smaller source terms.

Quantifying the change in the source terms requires an understanding of how this change arises. We begin with the thermal source in (52). When the value for the radial field, $\bar{B}_r'$, is prescribed, we expect the thermal source to depend on Ra^*, $\bar{\mathbf{V}}$ and $\nabla \bar{T}'$ because the ratio L/R and derivatives with respect to x are the same for a given source (say $l = 2$). The amplitude of the temperature field is constrained to lie between 0 and 1, whereas the temperature gradient, $\nabla \bar{T}' \approx \bar{T}'/d_T'$, is characterized by a length scale, d_T'. Consequently, we predict that the dimensionless thermal source varies as

$$S_T' \propto Ra^* Ro/d_T' \tag{55}$$

where the Rossby number, Ro, is used to characterize the amplitude of the dimensionless velocity.

A similar treatment of the magnetic source suggests a dependence on $\bar{\mathbf{B}}'^2$ and a length d_M', which describes the gradient in the magnetic field. The parameters $\bar{B}_r'$ and N' are treated as known quantities, which are held fixed during the extrapolation. In this case the dimensionless magnetic source is expected to vary as

$$S_M' \propto \Lambda E_\eta/d_M' \tag{56}$$

where we have used the Elssasser number, Λ, to characterize $\bar{\mathbf{B}}'^2$. Finally, the induction source depends on $\bar{\mathbf{V}}'$ and $\bar{\mathbf{B}}'$, as well as a length scale d_I' and a time scale $\tau_I' = d_I'/V'$, which is taken to be an advective timescale. Combining these results gives

$$S_I' \propto Ro^2 \Lambda^{1/2}/d_I'^2. \tag{57}$$

Aubert *et al.* (2017) argue that the length scales in (55)–(57) (denoted collectively as $d_\perp$) are nearly invariant once the dynamo solution reaches a MAC force balance with realistic values for Rm and Λ. Fixing these length scales allows us to predict the change in the amplitude of the sources from Solution 2 to Solution 1 using only the values from Table 1 (with $Ro = RmEPm^{-1}$). The results can be compared with direct calculations noted above. According to (55)–(57) the dimensionless thermal, magnetic and induction sources increase by 3.79×, 3.56× and 3.82×, respectively. While these changes are somewhat smaller than the actual change in the source terms, we might attribute the discrepancy to a modest change in the length scales. If these length scales cease to change as much in a magnetostrophic balance when E is reduced, it might be

Downloaded from https://academic.oup.com/gji/article-abstract/212/3/1523/4628047
by University of California, Berkeley/LBL user
on 19 January 2018

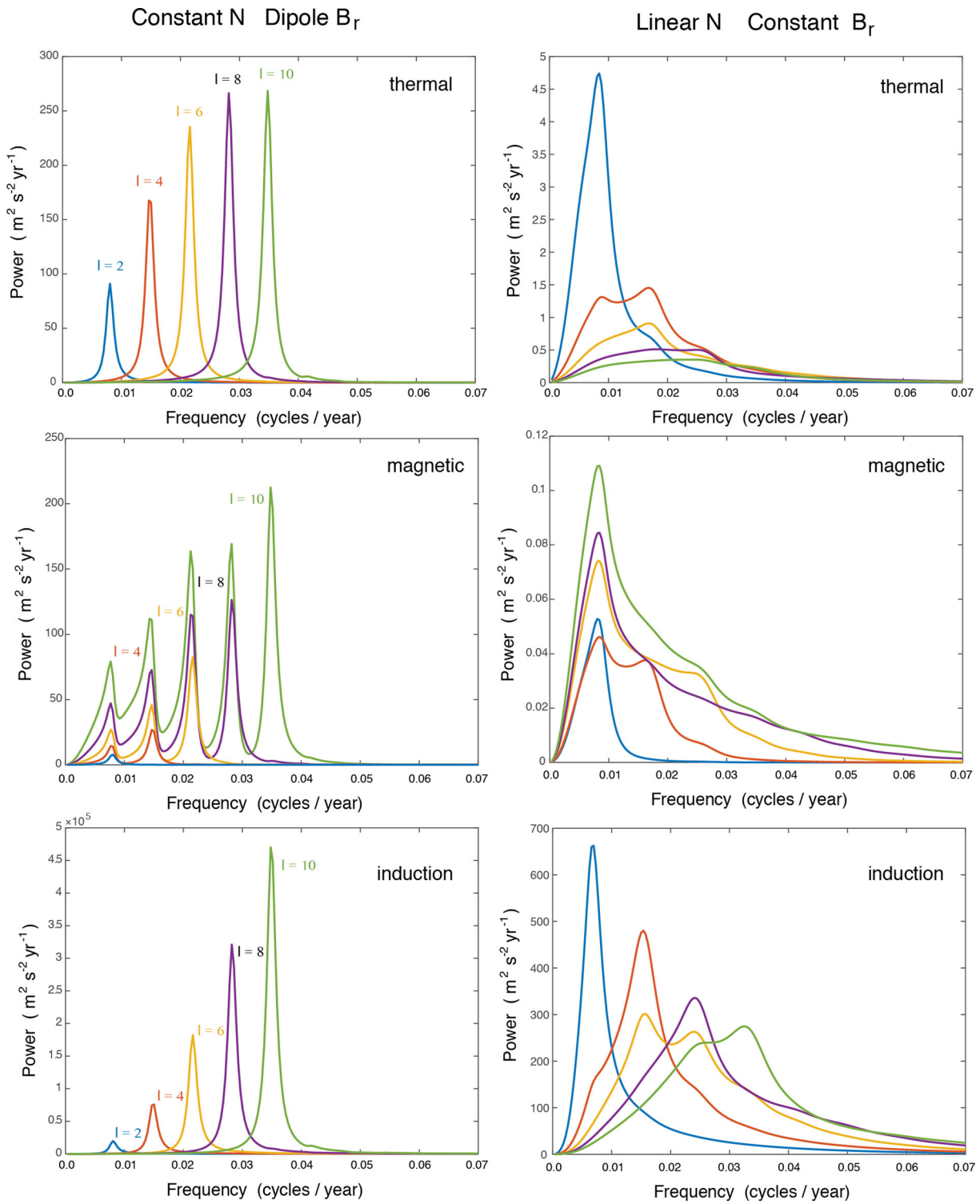

Figure 5. Power spectra for predicted wave velocity v_ϕ at the top of the core. Thermal, magnetic and induction sources are considered in rows 1, 2 and 3, respectively. Two different models for the layer properties are adopted in the calculations. Column 1 shows results for a layer with constant stratification $N = 0.84\,\Omega$ and a dipolar radial field $\bar{B}_r$ with a peak amplitude of 0.62 mT. Column 2 shows results for a layer with linearly varying N and a constant radial field $\bar{B}_r = 0.62$ mT. Even degree forcing $l = 2, 4, 6, 8, 10$ is responsible for symmetric v_ϕ about the equator. The mean square velocity (in m^2 s^{-2}) is obtained by integrating the power spectra over frequency.

reasonable to assume that these discrepancies will become less important as Earth-like conditions are approached.

Another test of the prediction is afforded by the results of Solution 3, where only *Pm* is changed in the input parameters. We observe a small change in the output for *Rm* (and hence *Ro*), whereas a large change occurs in Λ. Using the values from Table 1 to scale the sources, we predict changes of 0.90×, 1.74× and 1.87× in the thermal, magnetic and induction terms. By comparison, the actual

Downloaded from https://academic.oup.com/gji/article-abstract/212/3/1523/4628047
by University of California, Berkeley/LBL user
on 19 January 2018

change in the sources computed from the dynamo model is 0.97×, 1.51× and 2.90 ×. The largest discrepancy occurs in the induction source, which is most sensitive to a change in length scale.

We proceed by assuming that changes in the length scales are small. The resulting proportionalities from (55) to (57) are then used to extrapolate to Earth-like conditions. A representative state for the core is defined by setting $\tilde{V}_{\rm rms} = 0.38$ mm s^{-1} (Holme 2015), $\tilde{B}_{\rm rms} = 2.5$ to 4 mT (Buffett 2010; Gillet *et al.* 2010) and $\Delta T = 10$ mK (King *et al.* 2010). These values correspond to dimensionless parameters $Ro = 2 \times 10^{-6}$, $\Lambda = 10$ to 20 and $Ra^* = 8 \times 10^{-5}$. Using $\Lambda = 10$ along with the other estimates for the state of the core in (55) to (57) suggest that the source terms from Solution 2 should be reduced by 1.8×10^{-6}, 1×10^{-3} and 1×10^{-6} at Earth-like conditions. It follows that the rms amplitude of waves produced by thermal, magnetic and induction sources become 6×10^{-7} m s^{-1}, 8×10^{-5} m s^{-1} and 6×10^{-6} m s^{-1}. The largest wave amplitude is due to the magnetic source, and it yields an amplitude of roughly 2 km yr^{-1}. This result is remarkably consistent with observations.

Several things could alter the preceding estimates. First, convective temperature anomalies are predicted to become smaller as conditions become more realistic (Aubert *et al.* 2017). Such small anomalies would not penetrate as deeply into the stratified layer and the source would be confined to the lowermost region of the stratified layer. As a consequence, we expect a substantial decrease in the amplitude of the predicted wave due to the thermal source. This change would make the thermal source even weaker than our initial estimate. By comparison, magnetic and induction sources are more likely to penetrate deeply into the layer because of the influence of horizontal flow inside the layer on the radial magnetic field. A second consideration concerns the uncertainty in estimates for Λ. Numerical models that achieve realistic values for $Rm = 10^3$ often produce values for Λ between 20 and 30 (Aubert *et al.* 2017), depending on the nature of the convective forcing (see Solution 5). Larger values for Λ (relative to our choice of $\Lambda = 10$) would imply a larger wave amplitude for both magnetic and induction sources, although the greatest increase occurs in the magnetic source. Thus the magnetic source would remain the largest of the three sources. Allowing for larger Λ might increase the predicted wave amplitude by a factor of three larger relative to the value given above. However, this change is likely within the uncertainty of the extrapolation.

6 CONCLUSIONS

We examine the influence of convection and magnetic-field generation on the excitation of MAC waves in Earth's core. Three viable source mechanisms are identified in this study, including the effects of thermal buoyancy, Lorentz forces and magnetic induction. Each of these sources is evaluated using a dynamo model and the results are represented using a simple parametric description of the power spectrum. All of these source spectra produce unrealistically large wave velocities when we adopt realistic physical properties in the wave equation. This inconsistency arises because the source terms are computed from a dynamo models that necessarily relies on unrealistic physical properties. When estimates of the source terms are extrapolated to Earth-like conditions, we find that the Lorentz force emerges as the primary excitation source. This source is expected to produce wave velocities of $\approx$2 km yr^{-1} when the Elsasser number is $\Lambda \approx 10$ and $Rm \approx 10^3$.

Power spectra for the predicted wave velocities depend on the nature of stratification at the top of the core. A layer with a constant stratification and a dipole magnetic field yields sharply peaked power spectra at frequencies corresponding to individual MAC waves and their radial overtones. By comparison, a layer with linear varying stratification and a constant background magnetic field produces a broader, more distributed spectrum with most of the power between periods of 30 and 100 yr. Waves at shorter periods would have shorter wavelengths and would be more difficult to detect in magnetic-field variations at Earth's surface. Much of the difference in wave behaviour can be attributed to a more complex wave structure when the strength of stratification varies across the layer. The absence of sharp peaks in estimates of core-surface flow at periods below 100 yr (Jackson 1997; Gillet *et al.* 2009) would seem to argue against a constant layer stratification and a simple dipolar radial magnetic field. On the other hand, a more diffuse spectrum associated with a radially varying stratification and a constant radial field is compatible with layer properties inferred by fitting MAC waves to estimates of core-surface flow (Buffett *et al.* 2016).

ACKNOWLEDGEMENTS

This work is partially supported by the National Science Foundation (grant EAR-1430526). We thank Julien Aubert and an anonymous reviewer for comments and suggestions that substantially improved the paper.

REFERENCES

Aubert, J., Gastine, T. & Fournier, A., 2017. Spherical convective dynamos in the rapidly rotating asymptotic regime, *J. Fluid Mech.,* **813,** 558–593.

Bouligand, C., Gillet, N., Jault, D., Schaeffer, N., Fournier, A. & Aubert, J., 2016. Frequency spectrum of the geomagnetic field harmonic coefficients from dynamo simulations, *Geophys. J. Int.,* **207,** 1142–1157.

Braginsky, S.I., 1993. MAC-oscillations of the hidden ocean of the core, *J. Geomagn. Geoelectr.,* **45,** 1517–1538.

Buffett, B.A., 2010. Tidal dissipation and the strength of the Earth's internal magnetic field, *Nature,* **468,** 952–954.

Buffett, B., 2014. Geomagnetic fluctuations reveal stable stratification at the top of the Earth's core, *Nature,* **507,** 484–487.

Buffett, B., Knezek, N. & Holme, R., 2016. Evidence for MAC waves at the top of Earth's core and implications for variations in length of day, *Geophys. J. Int.,* **204,** 1789–1800.

Christensen, U.R. & Aubert, J., 2006. Scaling properties of convection-driven dynamos in rotating spherical shells and application to planetary magnetic fields, *Geophys. J. Int.,* **166,** 97–114.

Christensen, U.R., Aubert, J. & Hulot, G., 2010. Conditions for Earth-like geodynamo models, *Earth planet. Sci. Lett.,* **296,** 487–496.

Christensen, U.R., Wardinski, I. & Lesur, V., 2012. Timescales of geomagnetic secular acceleration in satellite field models and geodynamo models, *Geophys. J. Int.,* **190,** 243–254.

Davidson, P.A., 2013. Scaling laws for planetary dynamos, *Geophys. J. Int.,* **195,** 67–74.

Farrell, B.F. & Ioannou, P.J., 1993. Stochastic forcing of the linearized Navier-Stokes equation, *Phys. Fluids,* **5,** 200–220.

Gillet, N., Pais, M.A. & Jault, D., 2009. Ensemble inversion of time-dependent core flow models, *Geochem. Geophys. Geosyst.,* **10,** Q06004, doi:10.1029/2008GC002290.

Gillet, N., Jault, D., Canet, E. & Fournier, A., 2010. Fast torsional waves and strong magnetic field within the Earth's core, *Nature,* **465,** 74–77.

Gillet, N., Jault, D. & Canet, E., 2017. Excitation of travelling torsional normal modes in an Earth's core model, *Geophys. J. Int.,* **210,** 1503–1516.

Gomi, H., Hirose, K., Akai, H. & Fei, Y.W., 2016. Electrical resistivity of substitutionally disordered hcp Fe-Si and Fe-Ni alloys: chemically-induced resistivity saturation in the Earth's core, *Earth planet. Sci. Lett.,* **451,** 51–61.

Downloaded from https://academic.oup.com/gji/article-abstract/212/3/1523/4628047
by University of California, Berkeley/LBL user
on 19 January 2018

Gubbins, D., Thompson, C.J. & Whaler, K.A., 1982. Stable regions in the Earth's liquid core, *Geophys. J.R. astr. Soc.,* **68,** 241–251.
Holme, R., 2015. Large-scale flow in the core, in *Treatise on Geophysics,* 2nd edn, vol. 8, pp. 91–113, ed. Schubert, G. & Elsevier, B.V.
Houdek, G., Balmforth, N.J., Christensen-Dalsgaard, J. & Gough, D.O., 1999. Amplitude of stochastically excited oscillations in main-sequence stars, *Astron. Astrophys.,* **351,** 582–596.
Jackson, A., 1997. Time-dependency of tangentially geostrophic core surface motions, *Phys. Earth planet. Inter.,* **103,** 293–311.
Jaupart, E. & Buffett, B., 2017. Generation of MAC waves by convection in Earth's core, *Geophys. J. Int.,* **209,** 1326–1336.
Jones, C.A., 2011. Planetary magnetic fields and fluid dynamos, *Annu. Rev. Fluid Mech.,* **43,** 583–614.
King, E.M., Soderlund, K.M., Christensen, U.R., Wicht, J. & Aurnou, J., 2010. Convective heat transfer in planetary dynamo models, *Geochem. Geophys. Geosyst.,* **11,** Q06016, doi:10.1029/2010GC003053.
Lecoanet, D., Le Bars, M., Burns, K.J., Vasil, G.M., Brown, B.P., Quataert, E. & Oishi, J.S., 2015. Numerical simulations of internal wave generation by convection in water, *Phys. Rev. E,* **91,** doi:10.1103/PhysRevE.91.063016.
Lhuillier, F., Fournier, A., Hulot, G. & Aubert, J., 2011. The geomagnetic secular-variation timescale in observations and numerical dynamo models, *Geophys. Res. Lett.,* **38,** L09306, doi:10.1029/2011GL047356.
Lighthill, M.J., 1952. On sound generation aerodynamically. I. General Theory, *Proc. R. Soc. A,* **211,** 564–587.
Matsui, H., King, E. & Buffett, B., 2014. Multiscale convection in a geodynamo simulation with uniform heat flux along the outer boundary, *Geochem. Geophys. Geosyst.,* **15,** 3212–3225.
Olson, P., Maylis, L. & Reynolds, E., 2017. Dynamo tests for stratification below the core-mantle boundary, *Phys. Earth planet. Inter.,* **271,** 1–18.
Pedlosky, J., 1987. *Geophysical Fluid Dynamics,* 2nd edn, Springer-Verlag, p. 715.
Pozzo, M., Davies, C., Gubbins, D. & Alfe, D., 2012. Thermal and electrical conductivity of iron at Earth's core conditions, *Nature,* **485,** 355–358.
Rice, S.O., 1954. Mathematical analysis of random noise, in *Selected Papers on Noise and Stochastic Processes,* pp. 133–294, ed. Wax, N., Dover.
Stein, R.F., 1967. Generation of acoustic and gravity waves by turbulence in an isothermal stratified atmosphere, *Sol. Phys.,* **2,** 385–432.
Wang, M., Freund, J.B. & Lele, S.K., 2006. Computational prediction of flow-generated sound, *Annu. Rev. Fluid Mech.,* **38,** 483–512.
Yadev, R., Gastine, T., Christensen, U.R., Wolk, S.J. & Poppenhaeger, K., 2016. Approaching a realistic force balance in geodynamo simulations, *Proc. Natl. Acad. Sci. USA,* **113,** 12 065–12 070.

APPENDIX A: DERIVATION OF WAVE EQUATION

Braginsky (1993) derived a scalar wave equation for zonal MAC waves from the nearly geostrophic equations of motion in (14)–(16). The original treatment was restricted to a dipolar background magnetic field, but the approach can be extended to other background fields. The starting point is the solenoidal condition $\nabla \cdot \mathbf{v} = 0$, which can be approximated in a thin layer as

$$\frac{\partial v_r}{\partial r} + \frac{1}{R \sin\theta} \frac{\partial (\sin\theta \, v_\theta)}{\partial \theta} = 0, \tag{A1}$$

where R is the radius of the CMB. Substituting for v_θ from (16) and integrating over radius yields

$$v_r = -\left(\frac{1}{2\Omega R \rho_0 \mu}\right) \frac{1}{\sin\theta} \frac{\partial}{\partial \theta} \left(\frac{\sin\theta \, B_r b_\phi}{\cos\theta}\right) - \frac{1}{2\Omega R \sin\theta} \frac{\partial}{\partial \theta} \left(\frac{\sin\theta \, F_M}{\cos\theta}\right), \tag{A2}$$

where

$$F_M(r,\theta) = \int_R^r f_M(r',\theta) \, \mathrm{d}r' \tag{A3}$$

and the integration constant is evaluated using the boundary conditions $v_r = b_\phi = 0$ at $r = R$.

Eliminating pressure P from (14) and (15) relates the azimuthal flow v_ϕ to the buoyancy force $g\rho'$. Substituting for v_ϕ in the ϕ component of the induction in (17) gives

$$\frac{\partial b_\phi}{\partial t} - \eta \frac{\partial^2 b_\phi}{\partial r^2} = \left(\frac{B_r}{2\Omega R \cos\theta}\right) \left[\frac{\partial f_T}{\partial \theta} - \frac{1}{\rho_0} \frac{\partial (g\rho')}{\partial \theta}\right] + f_I, \tag{A4}$$

where g can be approximated as a constant. Taking the time derivative of (A4) and substituting for the time derivative of ρ' from (5) gives

$$\frac{\partial^2 b_\phi}{\partial t^2} - \eta \frac{\partial^3 b_\phi}{\partial r^2 \partial t} = \left(\frac{B_r}{2\Omega R \cos\theta}\right) \frac{\partial}{\partial \theta} \left[\dot{f}_T - N^2 v_r\right] + \dot{f}_I, \tag{A5}$$

where $\dot{f}_T$ and $\dot{f}_I$ represent time derivatives of the forcing terms and

$$N^2(r,\theta) = -\frac{g}{\rho_0} \frac{\partial \bar{\rho}}{\partial r} \tag{A6}$$

is the squared buoyancy frequency. The final step is to substitute for v_r into (A5) to obtain

$$\frac{\partial^2 b_\phi}{\partial t^2} - \eta \frac{\partial^3 b_\phi}{\partial r^2 \partial t} - \left(\frac{B_r N^2}{4\Omega^2 R^2}\right) \mathcal{L}_\theta^2 \left(\frac{B_r b_\phi}{\rho_0 \mu}\right) = S_T + S_M + S_I, \tag{A7}$$

where the operator $\mathcal{L}_\theta^2$ is defined in (19) and the source terms S_T, S_M and S_I are given in (20)–(22). The specific form of (A7) depends on N^2 being independent of colatitude θ. Retaining the θ dependence would require a straightforward modification of the operator $\mathcal{L}_\theta^2$.

APPENDIX B: SPATIAL FORM OF SOURCE TERMS

Expressions for the source terms are dictated by the use of spherical harmonic expansions in the dynamo model. For example, the thermal source involves $\bar{\nabla}' \cdot \nabla' \bar{T}'$, which can be expanded in Legendre polynomials, $P_l^0(x)$, as

$$\bar{\nabla}' \cdot \nabla' \bar{T}' = \sum_l s_l(r,t) P_l^0(x), \tag{B1}$$

where $s_l(r,t)$ is the known amplitude from the dynamo model. We confine our attention to Legendre functions with $m = 0$ because the waves are zonal. Substituting (B1) into the definition of the thermal source in (52) defines the dependence on x as

$$B_r'(x) \frac{\sqrt{1-x^2}}{x} \frac{\partial}{\partial x} (\bar{\nabla}' \cdot \nabla' \bar{T}') = \bar{B}_r'(x) \, s_l(r,t) \left(\frac{P_l^1(x)}{x}\right). \tag{B2}$$

This source is well defined for even l (and hence symmetric waves), but it exhibits a singularity at the equator $x = 0$ for odd l. This singularity arises because the Coriolis force vanishes at the equator. Adopting a dipole radial magnetic field, $\bar{B}_r'(x) = B_d \, x$, eliminates this singularity because the Lorentz force vanishes together with the Coriolis force at the equator (see eq. 16). Apart from this rather special case, the magnetic perturbation b_ϕ must vanish at the equator. This outcome is borne out by numerical solutions of the wave equation. Consequently, the singularity in the source corresponds to a node in the waves; the projection of the source onto the wave leads to a well-defined response.

Another point of elaboration arises in the description of the magnetic source. The Lorentz force in the dynamo model is represented

Downloaded from https://academic.oup.com/gji/article-abstract/212/3/1523/4628047
by University of California, Berkeley/LBL user
on 19 January 2018

by a toroidal vector field

$$f'_M(r,x,t) = \hat{\phi}\cdot(\bar{\mathbf{B}}'\cdot\nabla'\bar{\mathbf{B}}') = -\sum_l \frac{t_l}{r}\partial_\theta P_l^0(\cos\theta) \approx \sum_l \frac{t_l(r,t)}{R}P_l^1(x), \tag{B3}$$

where $t_l(r, t)$ are the toroidal coefficients. Integrating f'_M over r to define F'_M retains the same spatial dependence on $P_l^1(x)$, so the magnetic source term in the wave equation is specified by $\mathcal{L}_x^2 P_l^1(x)$. Odd values for l in f'_M and F'_M produce symmetric forces and symmetric zonal flow (defined by v_ϕ). Evidence for this symmetry in f'_M within the stratified layer is seen in Fig. 2(b), particularly at low latitudes. Fig. 2(b) also shows that the Lorentz force is quite weak on the equator. However, $P_l^1(x)$ for an odd l does not vanish on the equator. Instead, a superposition of several harmonic components is needed to create a weak Lorentz force at the equator. A more convenient choice of basis functions for the source term is defined by writing f'_M as

$$f'_M(r,x,t) \approx \sum_l \frac{t_l(r,t)}{R}\left[P_l^1(x) - P_l^1(0)\right] + \sum_l \frac{t_l(r,t)}{R}P_l^1(0). \tag{B4}$$

Each term in the first summation now vanishes at the equator, while the second sum of terms is independent of x. Any non-zero value for f'_M at the equator is accommodated by the constant term, which does not effectively excite waves. Consequently, we define the spatial structure of the magnetic source using $\mathcal{L}_x^2[P_l^1(x) - P_l^1(0)]$. Fig. B1 shows the spatial structure of the magnetic source at $l = 5$ and the thermal source at $l = 4$ for the case of a constant background field. Similarities between these sources suggests that both are capable of exciting $l = 4$ waves.

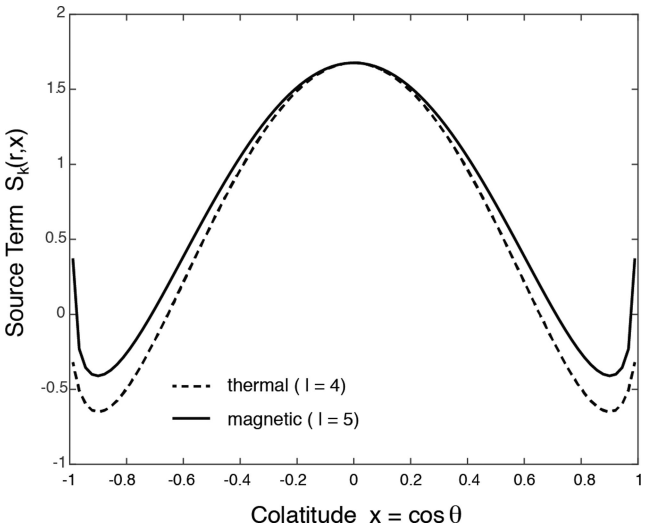

Figure B1. Thermal ($l = 4$) and magnetic ($l = 5$) sources as a function of $x = \cos\theta$. The amplitudes are normalized to facilitate comparison. Both sources are primarily responsible for generating $l = 4$ waves.

Downloaded from https://academic.oup.com/gji/article-abstract/212/3/1523/4628047
by University of California, Berkeley/LBL user
on 19 January 2018